optica

Terahertz investigation of bound states in the continuum of metallic metasurfaces

Xiaoguang Zhao,[1,3,†] Chunxu Chen,[1,†] Kelson Kaj,[2] Ian Hammock,[2] Yuwei Huang,[1] Richard D. Averitt,[2] and Xin Zhang[1,*]

[1]Department of Mechanical Engineering, Boston University, 110 Cummington Mall, Boston, Massachusetts 02215, USA
[2]Department of Physics, University of California, San Diego, 9500 Gilman Drive, La Jolla, California 92093, USA
[3]e-mail: zhaoxg@bu.edu
*Corresponding author: xinz@bu.edu

Received 11 August 2020; revised 18 September 2020; accepted 21 September 2020 (Doc. ID 404754); published 3 November 2020

The concept of "bound states in the continuum" (BIC) describes an idealized physical system exhibiting zero radiative loss composed, for example, of an infinitely extended array of resonators. In principle, vanishing of radiative losses enables an infinitely high-quality factor and corresponding infinite lifetime of the resonance. As such, BIC inspired metasurfaces and photonic designs aim to achieve superior performance in various applications including sensing and lasing. We describe an analytical model based on temporal coupled mode theory to realize an "accidental" (i.e., parameter-tuned) Friedrich–Wintgen BIC. Further, we experimentally verify this model with measurements of quasi-BICs in a metallic terahertz metasurface (MS) and the corresponding complementary metasurface (CMS) using terahertz time domain spectroscopy. For the MS and CMS structures, quality factors of ∼20 are achieved, limited by non-radiative intrinsic loss in the materials. Our results reveal that Babinet's principle qualitatively holds for the MS and CMS quasi-BIC structures. In addition, ultra-high electric and magnetic field enhancement MS and CMS structures, respectively, are presented.

https://doi.org/10.1364/OPTICA.404754

1. INTRODUCTION

High-quality factor (high-Q) optical resonators are in high demand in photonic systems due to rich physical phenomena associated with the lifetimes of such resonances [1], enabling a plethora of applications, such as enhanced light emission [2], chemical and biological sensing [3,4], and non-linear optics [5,6]. The bound state in the continuum (BIC) is one approach to achieve, in principle, infinite quality factors since the energy in the resonator is trapped without leakage to the continuum [7]. Ideal BICs may be considered as resonances with zero leakage and are referred as embedded trapped modes. There are two main approaches to achieve BICs. One approach is to create a symmetry-protected BIC where a trapped mode with a given symmetry is embedded into a continuum with a distinct symmetry, such that the leakage of the trapped mode is forbidden [8,9]. A second approach is to create an "accidental" BIC, where the parameters of the target system are tuned to achieve cancellation of outgoing waves to the continuum [10]. In optics and photonics, symmetry-protected and accidental BICs have been achieved in coupled waveguides [11,12], gratings [13], photonic crystals [14–16], photonic circuits [17–19], and metamaterials/metasurfaces (MM/MS) [20]. Photonic BICs have enabled an array of astonishing properties and applications, including enhanced lasing [21,22], gapless waveguides [23,24], and robust topological states [25,26].

MMs and MSs, as versatile constructs to design the effective properties of engineered materials, serve as a powerful platform to achieve BIC-like responses to manipulate electromagnetic waves. Due to the infinite lifetime and zero leakage of the ideal BIC, it is not possible to couple external excitations to the BIC. Indeed, ideal BICs are not observable in the electromagnetic spectrum [27]. However, by introducing structural perturbations into the metasurface supporting a BIC, quasi-BICs (identifiable by a high-Q resonant mode induced by the coupling of two low-Q modes) emerge in the far-field response. All-dielectric MMs and MSs have been designed based on the coupling of different resonance modes to achieve quasi-BICs ranging from microwave to infrared frequencies [27–30]. Recently, dynamic BICs have been demonstrated by photo-injection of carriers in all-dielectric MSs [31,32]. In addition, metallic MSs have been designed to achieve symmetry-protected BICs [33,34]. In the majority of BICs achieved by metallic metasurfaces, unit cells with inversion and π-rotation (C_2) symmetry were selected to generate symmetry-protected BICs, from which high-Q quasi-BICs were realized by symmetry breaking.

In this paper, we report on symmetric metallic MSs supporting accidental BICs due to the coupling of distinct resonant modes. By tuning the structural parameters of the metasurface unit cell (without breaking the symmetry), the BICs evolve to an observable quasi-BIC high-Q Fano resonance. We also investigate complementary metasurface (CMS) BIC structures and discuss

the validity of Babinet's principle. We elucidate the underlying physics of our accidental BICs using an analytical model based on coupled mode theory (CMT) and numerical simulations for the MS and CMS structures. In addition, we discuss the giant electric and magnetic field enhancement in MSs and CMSs, respectively. Our findings shed light on understanding accidental BICs in metallic MSs, providing a complementary perspective to symmetry-protected BICs in metallic MSs. As we demonstrate, BIC-inspired MS design is helpful in developing high-Q filters, detectors, and other functional devices. The theoretical modeling employed may be generalized to aid in the design of quasi-BICs at other frequency regions.

2. BIC BASED ON COUPLED RESONANCES

As shown in Fig. 1, coupled modes in a multi-resonant system may be employed to obtain a high-Q resonance and BICs [7]. A general temporal CMT model may be employed to describe the system with two modes that are coupled with two ports [35–38]:

$$\frac{d}{dt}\begin{bmatrix} a_1 \\ a_2 \end{bmatrix} = (j\Omega - \Gamma)\begin{bmatrix} a_1 \\ a_2 \end{bmatrix} + K\begin{bmatrix} s_{1+} \\ s_{2+} \end{bmatrix} = j\begin{bmatrix} \omega_{01} + j\gamma_1 & k + j\gamma_{12} \\ k + j\gamma_{21} & \omega_{02} + j\gamma_2 \end{bmatrix}\begin{bmatrix} a_1 \\ a_2 \end{bmatrix} + \begin{bmatrix} k_{11} & k_{12} \\ k_{21} & k_{22} \end{bmatrix}\begin{bmatrix} s_{1+} \\ s_{2+} \end{bmatrix}, \quad (1)$$

where $[a_1,\ a_2]^T$ are the resonance amplitude of modes supported by the system, ω_{01} (γ_1) and ω_{02} (γ_2) are resonant frequencies (decay rates) of the two modes, k represents the direct coupling rate between the two modes, γ_{12} ($=\gamma_{21}$) is the coupling coefficient generated by the damping, k_{ij} is the coupling coefficient between the mode i and the port j ($i,\ j \in \{1,\ 2\}$), and s_{1+} (s_{2+}) is the input wave amplitude from the port 1 (2). The outgoing waves from the excited resonance modes are

$$\begin{bmatrix} s_{1-} \\ s_{2-} \end{bmatrix} = \begin{bmatrix} r_d & t_d \\ t_d & r_d \end{bmatrix}\begin{bmatrix} s_{1+} \\ s_{2+} \end{bmatrix} + \begin{bmatrix} d_{11} & d_{12} \\ d_{21} & d_{22} \end{bmatrix}\begin{bmatrix} a_1 \\ a_2 \end{bmatrix}, \quad (2)$$

in which s_{1-} and s_{2-} are the outgoing wave amplitudes at ports 1 and 2, respectively; r_d and t_d are the direct reflection and transmission coefficient between the ports in the absence of the resonant modes; and d_{ij} is the coupling coefficient between the port j and the mode i ($i,\ j \in \{1,\ 2\}$). If the resonator is lossless, the decay rate is determined by the radiative loss, i.e., $\gamma_1 = \gamma_{r1}$ and $\gamma_2 = \gamma_{r2}$, where γ_{r1} and γ_{r2} are the radiation losses for modes 1 and 2, respectively. The terms γ_{r1} and γ_{r2} are related to the radiative quality factors (Q_{r1} and Q_{r2}) of the resonance by $\gamma_{r1} = \omega_{01}/(2Q_{r1})$ and $\gamma_{r2} = \omega_{02}/(2Q_{r2})$. Due to the symmetry of the system, $\gamma_{12} = \gamma_{21} = \sqrt{\gamma_1\gamma_2}$. When the input wave is incident from port 1, the transmission coefficient from port 1 to port 2 may be calculated by $t_{21}(\omega) = s_{2-}/s_{1+}$. Details of the derivation may be found in Supplement 1.

Within the framework of CMT, we may calculate the transmission coefficient of the uncoupled individual modes and the coupled modes. For each individual mode, a minimum appears in the transmission at the resonant frequency (i.e., ω_{01} and ω_{02}). As shown in Fig. 1(b), when the two modes couple to each other, the transmission spectrum possesses two minima and one maximum that manifests as a Fano response [27]. The minima correspond to the resonant frequency of each mode, and the maximum is induced by coupling between the two modes. The Hamiltonian of the coupled resonator is defined as $H \equiv j\Omega - \Gamma$, which exhibits two eigenvalues given by $(j\omega_- - \gamma_-)$ and $(j\omega_+ - \gamma_+)$. The imaginary parts of the complex eigenvalues are resonant frequencies of hybrid eigenmodes, while the real parts are decay rates of the hybrid eigenmodes. The first eigenmode corresponds to the maximum in the transmission coefficient, with quality factor $Q_- = \omega_-/(2\gamma_-)$. The second eigenmode is dampened by the high decay rate $[\omega_+/(2\gamma_+) < 1]$. Detailed discussion can be found in Supplement 1. Of note, the Fano transmission resonance exhibits a much higher quality factor than either of the original two modes.

The Fano resonance may shift with the frequency detuning between the resonant modes ($\delta\omega = \omega_{01} - \omega_{02}$) as shown in Figs. 1(c) and 1(d). When the Friedrich–Wintgen condition is met (i.e., $k(\gamma_1 - \gamma_2) = \sqrt{\gamma_1\gamma_2}\delta\omega$), the eigenvalue of one eigenmode becomes purely imaginary, indicating the radiative loss is zero with the mode being promoted to the status of a BIC [39]. Intuitively, the radiation from the two modes interfere to cancel the outgoing waves, forming an infinite lifetime resonance at the BIC frequency. Notably, for an ideal BIC, electromagnetic waves do not couple into the resonator. As such, it is impossible to excite or probe the BIC. However, the approach toward BIC status can (as a function of tuning some parameter) be identified as an increase in the quality factor, ultimately manifesting as the absence of an eigenmode resonance, as shown in Fig. 1(d). Practically speaking,

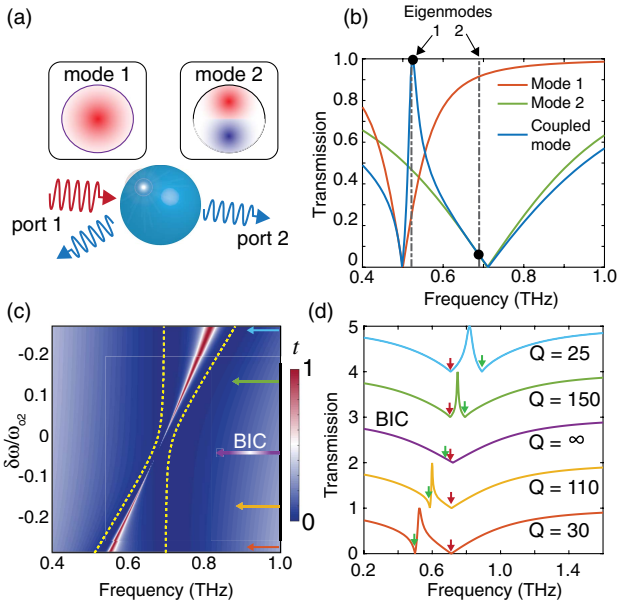

Fig. 1. Illustration of the generation of bound states in continuum (BICs) via coupled resonant modes. (a) Schematic of a resonating system supporting two modes coupled to two ports. (b) Theoretical transmission of uncoupled modes (red line, green line) and coupled modes (blue line with eigenfrequencies indicated with black dots) based on CMT. The first hybrid eigenmode corresponds to the high-Q transmission peak. (c) Color plot showing the shift of the resonance response for different frequency detuning. When the Friedrich–Wintgen condition is met, the BIC is achieved, and the resonant transmission peak vanishes (as identified by the purple arrow). The yellow dashed lines are the frequency of the resonant modes corresponding to minima of the transmission spectra. (d) The transmission coefficient for different frequency detunings labeled in (c) (color coded arrows). At the BIC, the quality factor is infinite. In (d), the green arrows label ω_{01} and the red arrows label ω_{02}. For the calculation, $Q_{r1} = 3$, $\omega_{02} = 2\pi \times 0.71$ THz, $Q_{r2} = 1$, $k = 2\pi \times 0.02$ THz, and ω_{01} is changing from $2\pi \times 0.53$ THz to $2\pi \times 0.89$ THz.

in the vicinity of the BIC (i.e., for quasi-BIC modes) the quality factor of the resonance is very high, and a sharp transmission peak may be obtained.

3. TERAHERTZ BIC-INSPIRED METALLIC MS AND CMS

In order to experimentally realize a quasi-BIC response from coupled resonances, we designed a MS comprised of split-ring resonators. Our structures are resonant at terahertz (THz) frequencies and, as shown in Fig. 2(a), possess an inductance-capacitance (LC) mode and a dipole mode. This structure is inspired by a MM supporting a high-Q anapole resonant mode in the microwave regime [40]. In our structure, the resonant frequency of the LC mode may be tuned by changing the middle gap (g), with little effect on the resonant frequency of the dipole mode. With such a platform, we can control the frequency detuning between the two modes in the vicinity of the ideal BIC. Details of the geometry may be found in Supplement 1. We fabricated the metasurfaces on a 5-μm-thick polyimide thin film using standard photolithography and characterized the transmission response of the metasurfaces using terahertz time domain spectroscopy. In addition, we performed simulations using the finite element method (FEM) with CST Studio Suite 2019 to investigate the response and surface current distribution for different modes of the metasurface (refer to Supplement 1 for simulation details).

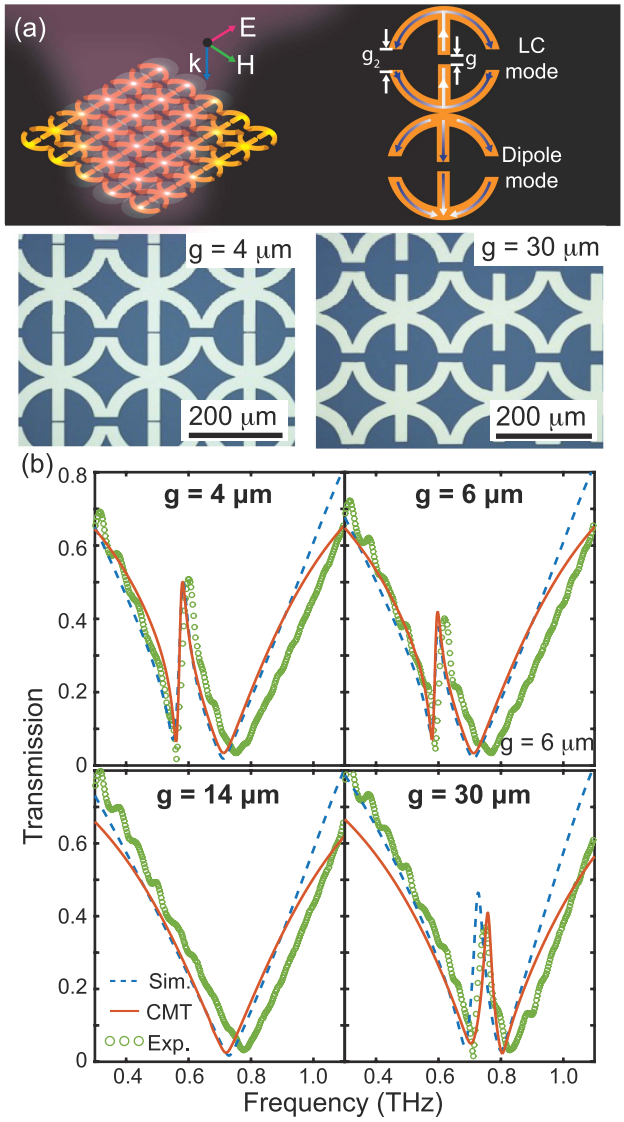

Fig. 2. Metallic MS structure and the results from experiments, simulation, and coupled mode theory. (a). The top is the schematic of the split-ring resonator MS. The left part displays an extended region of the arrays while the right portion illustrates the uncoupled resonant modes supported by the MS, in which arrows represents the surface current distribution extracted from simulation. The bottom column of (a) shows the microscopic images of the MS. (b) Transmission of the original MS as a function of frequency for different gap sizes (g), respectively. The green circles are the experimental data, the blue dashed line from the simulation, with the red line from coupled mode theory as discussed in the text.

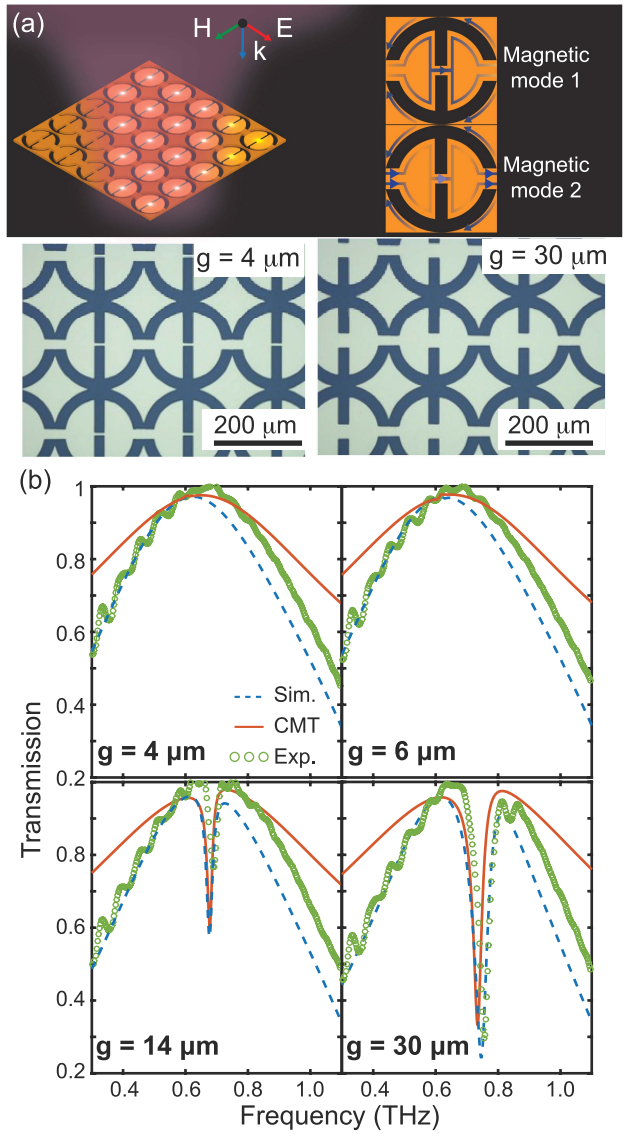

Fig. 3. Metallic CMS structure and the results from experiments, simulation, and coupled mode theory. (a) The top column is the schematic of the CMS. The left part displays an extended region of the arrays while the right portion illustrates the uncoupled resonant modes supported by the CMS, in which arrows represent the surface current distribution extracted from simulation. The bottom column of (a) shows microscopic images of the CMS. (b) Transmission of the CMS as a function of frequency for different gap sizes (g). The green dots are the experimental data, the blue dashed line the simulations, with the red line from coupled mode theory as discussed in the text.

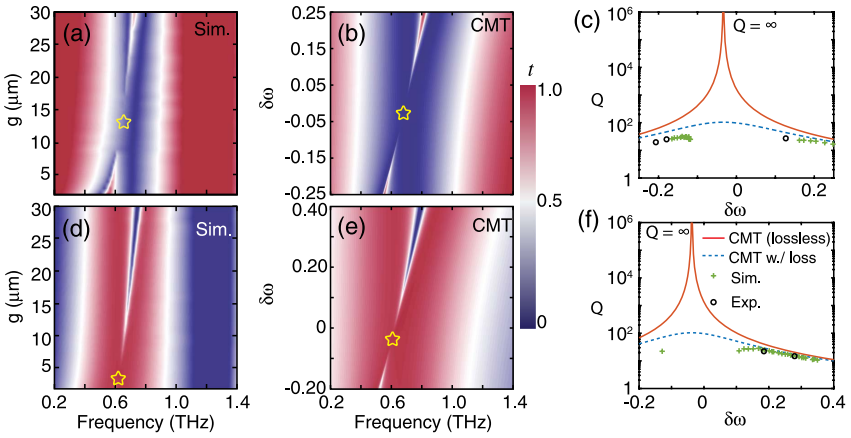

Fig. 4. Parametric study of quasi-BICs response for MS and CMS structures in the vicinity of the BIC frequency. (a) Color plot of the simulated transmission spectra with different gap sizes for the MS. (b) CMT transmission spectra with different frequency detuning for the MS. (d) and (e) show the corresponding color plots for the CMS structure. (c) Theoretical, simulated, and measured quality factors for the MS as a function of frequency detuning (CMT) or gap size (experiment, simulation). (f) The quality factors for the CMS. In (c) and (f), the frequency detuning is calculated by the frequency difference of the two minima (maxima) in the transmission of the MSs (CMSs) in the vicinity of the quasi-BIC frequency. BIC points are labeled by yellow stars in (a), (b), (d), and (e).

As shown in Fig. 2(b), when the middle gap size is 4 μm, a quasi-BIC Fano peak is observed with a transmission coefficient of 0.51 and quality factor of ∼20. The simulated spectrum agrees well with the experimental results. The current distribution indicates that the first transmission minimum is a LC mode and the second is a dipole mode. The transmission peak at 0.6 THz is the result of coupling between the LC and dipole modes and is the quasi-BIC mode. Since the LC and dipole modes couple to each other through the resonance and the leakage channel, the quasi-BIC mode features a Fano line shape as predicted from theoretical calculations [Fig. 1(b)] [20]. As the gap is increased, the LC mode shifts to higher frequencies, approaching the dipole resonant frequency. The decrease of the frequency detuning ($|\delta\omega|$) leads to a decrease of transmission peak value and an increase of the quality factor. The BIC may be identified by the vanishing of the Fano transmission peak when the gap size is 14 μm. When the BIC condition is broken by further increasing the gap size, a transmission peak reappears with a quality factor of 27. Of note, unlike the symmetry-protected BICs demonstrated in metallic metasurfaces [33,34], the quasi-BICs in the present structure are achieved by changing the gap size without breaking either C_2 or mirror symmetry of the metasurface.

The quasi-BIC achieved by the MS shown in Fig. 2(a) acts as a high-Q bandpass THz filter. According to the Babinet's principle [41], the corresponding CMS may be used to realize high-Q bandstop filters. As shown in Fig. 3(a), the CMS was designed and fabricated to investigate Babinet's principle in quasi-BIC structures. We formed the CMS by interchanging portions of the metal screen and gap in original metasurface structures and keeping the dimensions the same. As illustrated in Fig. 3(a), the CMS supports two magnetic modes, as indicated by the simulations. The coupling of these two modes may lead to the BIC and quasi-BICs, which exhibit a high-Q bandstop response. For a gap size of 30 μm, a transmission minimum is achieved at 0.75 THz with a quality factor of 15, as shown in Fig. 3(b). As the gap size is decreased, the transmission resonance strength decreases, and the quality factor increases. For gap sizes of 6 μm and 4 μm, the resonant mode of transmission minimum vanishes, indicative of ideal BIC behavior. Like the original metasurface, the BIC is also formed due to coupling between two modes under the Friedrich–Wintgen condition. However, a comparison between the quasi-BIC responses of the MS and CMS indicates that Babinet's principle only holds qualitatively.

According to Babinet's principle, the transmission of the original and complementary metasurfaces should satisfy $t_{21}(\omega) + t_{21c}(\omega) = 1$, in which t_{21c} is the transmission coefficient of the CMS, where the polarizations of the THz sources are dual and the metal is perfectly electric conducting [41]. However, the summation is not equal to 1 in the transmission of our structures, especially at the BIC frequency. For $g = 4$ μm, the original metasurface exhibits a quasi-BIC with a transmission peak at 0.6 THz, while its complement is at the BIC point with transmission ∼1. We performed a parametric study of the MS and CMS transmission response by sweeping the gap size from 2 μm to 30 μm in the numerical simulation. As shown in Figs. 4(a) and 4(d), it can be more clearly seen that Babinet's principle does not quantitatively hold. The BIC is achieved when $g = 14$ μm for the original MS while it is $g = 4$ μm for the CMS. The reason for the mismatch is that the frequencies of the uncoupled modes for the MS and the CMS deviate from each other due to differences in the mode profiles arising from losses in the metal screen and dielectric substrate [42,43]. The BICs based on coupled resonances make the deviation more obvious than conventional metamaterials/metasurfaces that do not support BIC, as revealed quantitatively by the theoretical analysis based on CMT presented below.

In order to reveal the physics underlying the response of our MS and CMS structures, we employed CMT modeling [Eqs. (1) and (2)] to fit the experimental and simulated results. Even though the BIC can be identified in the experimental and simulated results, the response is further clarified using CMT as shown in Fig. 1(d). The peak value of the quasi-BIC mode is relatively low in the measured and simulated results, while the peak value of the BIC mode approaches 1 for the lossless theoretical model. To obtain a better fit to the experimental results, we introduce an intrinsic loss term

Table 1. Fitting Parameters for the MS

Design	ω_{01} ($\times 2\pi$ THz)	ω_{02} ($\times 2\pi$ THz)	Q_{i1}	Q_{r1}	Q_{i2}	Q_{r2}	k ($\times 2\pi$ THz)
$g = 4$ μm	0.563	0.709	80	3	25	1	0.02
$g = 6$ μm	0.583	0.709	80	3	25	1	0.02
$g = 14$ μm	0.681	0.709	80	3	25	1	0.02
$g = 30$ μm	0.800	0.709	80	3	25	1	0.02

Table 2. Fitting Parameters for the CMS

Design	ω_{01} ($\times 2\pi$ THz)	ω_{02} ($\times 2\pi$ THz)	Q_{i1}	Q_{r1}	Q_{i2}	Q_{r2}	k ($\times 2\pi$ THz)
$g = 4$ μm	0.615	0.640	80	3	25	1	0.02
$g = 6$ μm	0.625	0.640	80	3	25	1	0.02
$g = 14$ μm	0.717	0.640	80	3	25	1	0.02
$g = 30$ μm	0.800	0.640	80	3	25	1	0.02

in the decay rates of the uncoupled modes, i.e., $\gamma_1 = \gamma_{r1} + \gamma_{01}$ and $\gamma_2 = \gamma_{r2} + \gamma_{02}$, in which γ_{01} and γ_{02} are the decay rates due to energy dissipation in the resonator. As shown in Figs. 2(b) and 3(b), the CMT models (red lines) fit the experimental and simulated results quite well in the vicinity of the quasi-BIC modes, validating the theoretical model. For a best fit of the MS response, we fixed $\omega_{02} = 2\pi \times 0.71$ THz and the quality factors (Q_1 and Q_2) and coupling coefficient (k), while sweeping ω_{01} from $2\pi \times 0.56$ THz to $2\pi \times 0.81$ THz. Similarly, for the CMS sample, we fixed $\omega_{02} = 2\pi \times 0.64$ THz (with Q_1, Q_2, and k fixed as for the MS), while sweeping ω_{01} from $2\pi \times 0.615$ THz to $2\pi \times 0.81$ THz. Details of the fitting parameters are shown in Tables 1 and 2. Our CMT modeling supports the notion that the gap size at which the BIC frequency occurs is different for the MS and CMS structures.

The inclusion of the additional (yet realistic) intrinsic loss in the fabricated metasurfaces damps the quasi-BIC mode. In Fig. 4, we compare the FEM simulations and CMT modeling including such non-radiative losses. As shown in the parametric-sweep of the transmission response (using FEM modeling) for different gap sizes [Fig. 4(a) shows the MS and Fig. 4(d) shows the CMS], the quasi-BIC vanishes when g ranges from 10 μm to 15 μm for the MS and over the range 3 μm to 7 μm for the CMS. Using CMT, similar plots can be made as a function of the detuning parameter $\delta\omega$, as shown in Fig. 4(b) for the MS and Fig. 4(e) for the CMS. The inclusion of loss results in an extended detuning range where the quasi-BIC resonance vanishes, consistent with the FEM simulations.

For ideal BICs, the theoretical quality factor should approach infinity. However, the intrinsic losses in the MS and CMS induce finite quality factors. In such lossy BICs, the leakage of energy in the metasurface to the ports is zero. Instead, the loss mechanism arises from ohmic loss in the metal and, to a lesser extent, dielectric loss in the substrate. We calculated the quality factor as a function of $\delta\omega$ using CMT with and without losses. Figures 4(c) and 4(f) compare theoretical quality factors with the simulated and measured quality factors for both the MS and CMS. The good agreement further validates our theoretical model. The quality factors for the quasi-BICs close to the ideal BIC frequency cannot be measured as the resonance vanishes (even in the presence of loss). The theoretical prediction suggests that eliminating or decreasing intrinsic loss in the MS and CMS would significantly increase the quality factor of the quasi-BICs. For example, if the metasurface was made of superconducting material and operating below T_C, a higher quality factor could be obtained.

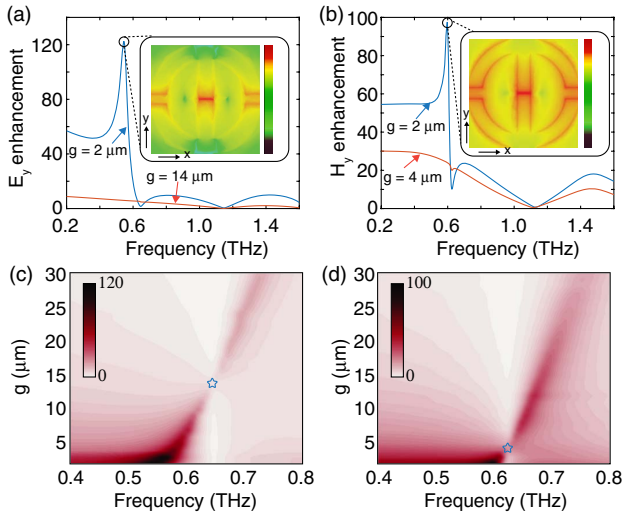

Fig. 5. Simulated field enhancement of the MS and CMS in quasi-BICs. (a) The electric field enhancement for the quasi-BIC response further away from the BIC point (blue) and close to the BIC (red) for the MS. (b) Corresponding magnetic field enhancement for the CMS. Insets in (a) and (b) are the near-field electric and magnetic field distribution for the MS and CMS, respectively. The arrows in the insets represent the surface current. (c) and (d) show color plots of the field enhancement for different gap sizes in the MS and CMS, respectively. BICs are labeled by blue stars.

Metasurfaces supporting quasi-BIC modes may provide large local field enhancement due to the high-Q resonance. For the MS, the electric field is confined in the gap regions, leading to strong electric field enhancement. As the simulations in Figs. 5(a) and 5(c) suggest, the quasi-BIC with $g = 2$ μm achieves a maximum E-field enhancement of ~120 at the resonant frequency of the hybrid mode. As the gap size increases, the E-field enhancement decreases. At the BIC point, the resonance of E-field enhancement disappears because the ingoing waves do not couple into the hybrid mode of the metasurface. As a result, for the quasi-BIC exhibiting the highest quality factor, the E-field enhancement is decreased. The MS acts as an "electric dipole" when driven by the electric field. According to Babinet's principle, the CMS modes correspond to a magnetic dipole. Therefore, the CMS exhibits magnetic field

(H-field) enhancement. As shown in Figs. 5(b) and 5(d), the CMS yields a maximum H-field enhancement of ~100 at the resonance frequency of the hybrid mode. Similar to the MS, the resonant enhancement vanishes at the BIC frequency. We conclude that it is possible to achieve E-field (H-field) enhancement using MS (CMS) structures in the quasi-BIC regime. We note that the BIC condition may be more clearly identified in the near-field spectrum in comparison to the far-field response, as evident by comparing Fig. 5(c) [5(d)] with Fig. 4(a) [4(b)].

4. CONCLUSION

In summary, we experimentally demonstrated a quasi-BIC resonance in a symmetric metasurface and the corresponding complementary structure. By tuning the gap without breaking the symmetry of the metasurface unit cell, coupling between the LC and dipole modes reduces the radiative loss of the hybrid mode when the Friedrich–Wintgen condition is approached. The roles of radiative loss and intrinsic losses were investigated using the FEM simulations and theoretical CMT modeling. Near the BIC frequency, two low-Q resonances couple to generate a high-Q hybrid resonant mode. We analytically revealed that the intrinsic loss in the BIC and quasi-BICs degrades the quality factor of the hybrid resonance. For structures supporting the BIC, Babinet's principle qualitatively holds between the metasurface and complementary metasurface due to modal profile differences arising from losses in the metal and dielectric regions of our structures. In addition, the quasi-BICs of the original metasurfaces exhibit a strong electric field enhancement while the complementary metasurfaces provide magnetic field enhancement. We also found that the near-field enhancement spectrum provides a potentially improved approach to identify the BIC condition in comparison to the far-field spectrum. The analytical model based on CMT provides a clear physical picture of the BIC based on coupled modes and may be generalized for other fields of wave physics including photonic crystals, photonic circuits, and acoustics, among others. THz quasi-BICs based on ultra-thin and flexible metasurfaces may be employed for filters, THz spectroscopy, chemical sensing, and other applications.

Funding. National Science Foundation Division of Electrical, Communications and Cyber Systems (NSF ECCS-1810252); Defense Advanced Research Projects Agency DRINQS Program (D18AC00014).

Acknowledgment. We acknowledge the Boston University Photonics Center for technical support.

Disclosures. The authors declare no conflicts of interest.

See Supplement 1 for supporting content.

[†]These authors contributed equally to this work.

REFERENCES

1. J. Lee, B. Zhen, S.-L. Chua, W. Qiu, J. D. Joannopoulos, M. Soljačić, and O. Shapira, "Observation and differentiation of unique high-Q optical resonances near zero wave vector in macroscopic photonic crystal slabs," Phys. Rev. Lett. **109**, 67401 (2012).
2. M. Fujita, S. Takahashi, Y. Tanaka, T. Asano, and S. Noda, "Simultaneous inhibition and redistribution of spontaneous light emission in photonic crystals," Science **308**, 1296–1298 (2005).
3. B. Luk'yanchuk, N. I. Zheludev, S. A. Maier, N. J. Halas, P. Nordlander, H. Giessen, and C. T. Chong, "The Fano resonance in plasmonic nanostructures and metamaterials," Nat. Mater. **9**, 707–715 (2010).
4. M. S. Luchansky and R. C. Bailey, "High-Q optical sensors for chemical and biological analysis," Anal. Chem. **84**, 793–821 (2012).
5. M. Kroner, A. O. Govorov, S. Remi, B. Biedermann, S. Seidl, A. Badolato, P. M. Petroff, W. Zhang, R. Barbour, B. D. Gerardot, R. J. Warburton, and K. Karrai, "The nonlinear Fano effect," Nature **451**, 311–314 (2008).
6. Y. Yang, W. Wang, A. Boulesbaa, I. I. Kravchenko, D. P. Briggs, A. Puretzky, D. Geohegan, and J. Valentine, "Nonlinear Fano-resonant dielectric metasurfaces," Nano Lett. **15**, 7388–7393 (2015).
7. C. W. Hsu, B. Zhen, A. D. Stone, J. D. Joannopoulos, and M. Soljačić, "Bound states in the continuum," Nat. Rev. Mater. **1**, 16048 (2016).
8. R. Parker, "Resonance effects in wake shedding from parallel plates: some experimental observations," J. Sound Vib. **4**, 62–72 (1966).
9. F. Dreisow, A. Szameit, M. Heinrich, R. Keil, S. Nolte, A. Tünnermann, and S. Longhi, "Adiabatic transfer of light via a continuum in optical waveguides," Opt. Lett. **34**, 2405–2407 (2009).
10. K. Koshelev, A. Bogdanov, and Y. Kivshar, "Meta-optics and bound states in the continuum," Sci. Bull. **64**(12), 836–842 (2019).
11. Y. Plotnik, O. Peleg, F. Dreisow, M. Heinrich, S. Nolte, A. Szameit, and M. Segev, "Experimental observation of optical bound states in the continuum," Phys. Rev. Lett. **107**, 183901 (2011).
12. X. Gao, B. Zhen, M. Soljačić, H. Chen, and C. W. Hsu, "Bound states in the continuum in fiber Bragg gratings," ACS Photonics **6**, 2996–3002 (2019).
13. J. M. Foley, S. M. Young, and J. D. Phillips, "Symmetry-protected mode coupling near normal incidence for narrow-band transmission filtering in a dielectric grating," Phys. Rev. B **89**, 165111 (2014).
14. C. W. Hsu, B. Zhen, J. Lee, S.-L. Chua, S. G. Johnson, J. D. Joannopoulos, and M. Soljačić, "Observation of trapped light within the radiation continuum," Nature **499**, 188–191 (2013).
15. M. Minkov, D. Gerace, and S. Fan, "Doubly resonant (2) nonlinear photonic crystal cavity based on a bound state in the continuum," Optica **6**, 1039–1045 (2019).
16. A. Taghizadeh and I.-S. Chung, "Quasi bound states in the continuum with few unit cells of photonic crystal slab," Appl. Phys. Lett. **111**, 31114 (2017).
17. C.-L. Zou, J.-M. Cui, F.-W. Sun, X. Xiong, X.-B. Zou, Z.-F. Han, and G.-C. Guo, "Guiding light through optical bound states in the continuum for ultrahigh-Q microresonators," Laser Photonics Rev. **9**, 114–119 (2015).
18. Z. Yu, X. Xi, J. Ma, H. K. Tsang, C.-L. Zou, and X. Sun, "Photonic integrated circuits with bound states in the continuum," Optica **6**, 1342–1348 (2019).
19. Z. Yu and X. Sun, "Acousto-optic modulation of photonic bound state in the continuum," Light Sci. Appl. **9**, 1–9 (2020).
20. M. F. Limonov, M. V. Rybin, A. N. Poddubny, and Y. S. Kivshar, "Fano resonances in photonics," Nat. Photonics **11**, 543–554 (2017).
21. A. Kodigala, T. Lepetit, Q. Gu, B. Bahari, Y. Fainman, and B. Kanté, "Lasing action from photonic bound states in continuum," Nature **541**, 196–199 (2017).
22. C. M. Gentry and M. A. Popović, "Dark state lasers," Opt. Lett. **39**, 4136–4139 (2014).
23. F. Benabid, J. C. Knight, G. Antonopoulos, and P. S. J. Russell, "Stimulated Raman scattering in hydrogen-filled hollow-core photonic crystal fiber," Science **298**, 399–402 (2002).
24. F. Couny, F. Benabid, P. J. Roberts, P. S. Light, and M. G. Raymer, "Generation and photonic guidance of multi-octave optical-frequency combs," Science **318**, 1118–1121 (2007).
25. B. Zhen, C. W. Hsu, L. Lu, A. D. Stone, and M. Soljačić, "Topological nature of optical bound states in the continuum," Phys. Rev. Lett. **113**, 257401 (2014).
26. H. M. Doeleman, F. Monticone, W. den Hollander, A. Alù, and A. F. Koenderink, "Experimental observation of a polarization vortex at an optical bound state in the continuum," Nat. Photonics **12**, 397–401 (2018).
27. A. A. Bogdanov, K. L. Koshelev, P. V. Kapitanova, M. V. Rybin, S. A. Gladyshev, Z. F. Sadrieva, K. B. Samusev, Y. S. Kivshar, and M. F. Limonov, "Bound states in the continuum and Fano resonances in the strong mode coupling regime," Adv. Photonics **1**, 1–12 (2019).

28. M. V. Rybin, K. L. Koshelev, Z. F. Sadrieva, K. B. Samusev, A. A. Bogdanov, M. F. Limonov, and Y. S. Kivshar, "High-Q supercavity modes in subwavelength dielectric resonators," Phys. Rev. Lett. **119**, 243901 (2017).
29. J. Tian, Q. Li, P. A. Belov, R. K. Sinha, W. Qian, and M. Qiu, "High-Q all-dielectric metasurface: super and suppressed optical absorption," ACS Photonics **7**, 1436–1443 (2020).
30. A. Overvig, N. Yu, and A. Alù, "Chiral quasi-bound states in the continuum," arXiv:2006.05484 (2020).
31. K. Fan, I. V. Shadrivov, and W. J. Padilla, "Dynamic bound states in the continuum," Optica **6**, 169–173 (2019).
32. S. Han, L. Cong, Y. K. Srivastava, B. Qiang, M. V. Rybin, A. Kumar, R. Jain, W. X. Lim, V. G. Achanta, S. S. Prabhu, Q. J. Wang, Y. S. Kivshar, and R. Singh, "All-dielectric active terahertz photonics driven by bound states in the continuum," Adv. Mater. **31**, 1901921 (2019).
33. D. R. Abujetas, N. van Hoof, S. ter Huurne, J. Gómez Rivas, and J. A. Sánchez-Gil, "Spectral and temporal evidence of robust photonic bound states in the continuum on terahertz metasurfaces," Optica **6**, 996–1001 (2019).
34. L. Cong and R. Singh, "Symmetry-protected dual bound states in the continuum in metamaterials," Adv. Opt. Mater. **7**, 1900383 (2019).
35. W. Suh, Z. Wang, and S. Fan, "Temporal coupled-mode theory and the presence of non-orthogonal modes in lossless multimode cavities," IEEE J. Quantum Electron. **40**, 1511–1518 (2004).
36. X. Zhao, J. Zhang, K. Fan, G. Duan, J. Schalch, G. Keiser, R. Averitt, and X. Zhang, "Real-time tunable phase response and group delay in broadside coupled split ring resonators," Phys. Rev. B **99**, 245111 (2019).
37. X. Zhao, G. Duan, K. Wu, S. W. Anderson, and X. Zhang, "Intelligent metamaterials based on nonlinearity for magnetic resonance imaging," Adv. Mater. **31**, 1905461 (2019).
38. E. N. Bulgakov and D. N. Maksimov, "Avoided crossings and bound states in the continuum in low-contrast dielectric gratings," Phys. Rev. A **98**, 053840 (2018).
39. H. Friedrich and D. Wintgen, "Interfering resonances and bound states in the continuum," Phys. Rev. A **32**, 3231–3242 (1985).
40. A. A. Basharin, V. Chuguevsky, N. Volsky, M. Kafesaki, and E. N. Economou, "Extremely high Q-factor metamaterials due to anapole excitation," Phys. Rev. B **95**, 35104 (2017).
41. H. Chen, J. F. O'Hara, A. J. Taylor, R. D. Averitt, C. Highstrete, M. Lee, W. J. Padilla, J. F. O. Hara, A. J. Taylor, R. D. Averitt, C. Highstrete, M. Lee, and W. J. Padilla, "Complementary planar terahertz metamaterials," Opt. Express **15**, 1084–1095 (2007).
42. F. Falcone, T. Lopetegi, M. A. G. Laso, J. D. Baena, J. Bonache, M. Beruete, R. Marqués, F. Martín, and M. Sorolla, "Babinet principle applied to the design of metasurfaces and metamaterials," Phys. Rev. Lett. **93**, 197401 (2004).
43. T. Zentgraf, T. P. Meyrath, A. Seidel, S. Kaiser, H. Giessen, C. Rockstuhl, and F. Lederer, "Babinet's principle for optical frequency metamaterials and nanoantennas," Phys. Rev. B **76**, 33407 (2007).